TPG-INR: Target Prior-Guided Implicit 3D CT Reconstruction for Enhanced Sparse-view Imaging

Qinglei Cao[†], Ziyao Tang[†] and Xiaoqin Tang^{*} Southwest University, China

cq118381505437@email.swu.edu.cn, ziyaotang03@outlook.com, tangx0530@swu.edu.cn

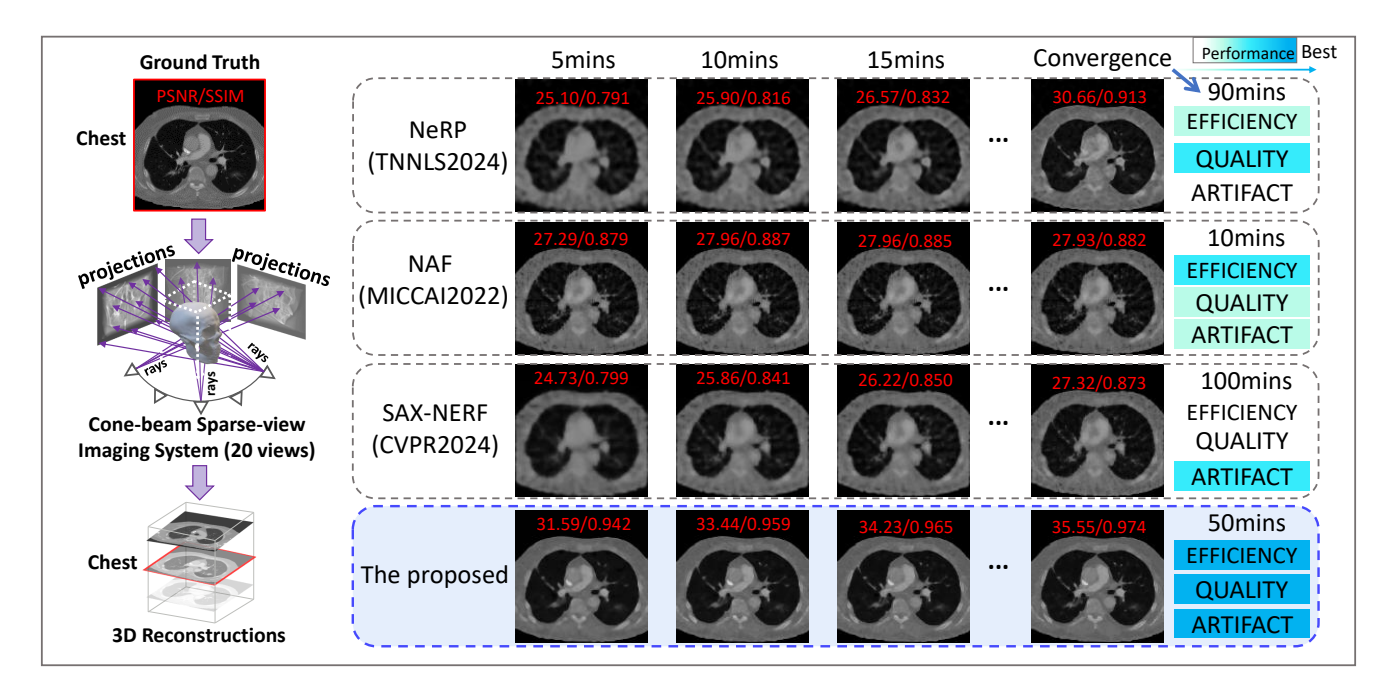


Figure 1. Sparse-view 3D CT reconstruction using the state-of-the-art methods. A comparative analysis with NeRP [27], NAF [38], and SAX-NeRF [5] highlights the superior performance of our method in learning efficiency, reconstruction precision, and artifact removal.

Abstract

X-ray imaging, based on penetration, enables detailed visualization of internal structures. Building on this capability, existing implicit 3D reconstruction methods have adapted the NeRF model and its variants for internal CT reconstruction. However, these approaches often neglect the significance of objects' anatomical priors for implicit learning, limiting both reconstruction precision and learning efficiency, particularly in ultra-sparse view scenarios. To address these challenges, we propose a novel 3D CT reconstruction framework that employs a 'target prior' derived from the object's projection data to enhance implicit learning. Our approach integrates positional and struc-

tural encoding to facilitate voxel-wise implicit reconstruction, utilizing the target prior to guide voxel sampling and enrich structural encoding. This dual strategy significantly boosts both learning efficiency and reconstruction quality. Additionally, we introduce a CUDA-based algorithm for rapid estimation of high-quality 3D target priors from sparse-view projections. Experiments utilizing projection data from a complex abdominal dataset demonstrate that the proposed model substantially enhances learning efficiency, outperforming the current leading model, NAF, by a factor of ten. In terms of reconstruction quality, it also exceeds the most accurate model, NeRP, achieving PSNR improvements of 3.57 dB, 5.42 dB, and 5.70 dB with 10, 20, and 30 projections, respectively. The code is available at https://github.com/qlcao171/TPG-INR.

^{1†}These authors contributed equally to this work.

^{2*}Corresponding author.

1. Introduction

X-rays, with superior penetration compared to natural light, enable visualization of internal structures, making them widely used in medical diagnosis, industrial testing, and security inspection [2, 14, 35]. However, the radiation from X-rays poses a cancer risk. Therefore, it is crucial to reduce the radiation dose while maintaining image quality in clinical diagnostics [4, 10]. To this end, this paper investigates methods for achieving rapid and high-quality CT reconstruction using a limited number of projections (only 10-30 projections) in both cone-beam and parallel-beam X-ray scanning scenarios, aiming to reduce radiation dose while providing reliable medical imaging support, thereby minimizing the harm of X-rays to the human body.

Our objective is to accurately reconstruct anatomy of organs or tissues from solely sparse-view projection data. Analytical reconstruction algorithms such as filtered back-projection (FBP) and Feldkamp-Davis-Kress (FDK) have the advantage of high speed, but the reconstructed results under sparse-view conditions often suffer from severe streak artifacts [9, 16, 32]. Iterative reconstruction algorithms, such as the Simultaneous Algebraic Reconstruction Technique (SART), typically converge faster but are highly sensitive to initial parameters and prone to streak artifacts that degrade reconstruction quality [16, 17, 26, 29, 30].

Recent advancements in deep learning have shown great potential for supervised learning in sparse-view CT (SVCT) reconstruction tasks [11, 19, 20, 28, 36, 39]. Jin et al. proposed FBPConvNet [15], which utilizes convolutional neural networks (CNN) to learn an end-to-end mapping from the projections to the images. However, acquiring paired CT data for training is challenging, and there is limited generalization ability across different anatomical regions. In 2020, Ben et al. proposed NeRF [21], introducing a novel implicit 3D reconstruction method. Compared to paired-learningbased methods, this approach not only avoids generalization issues arising from differences in data distribution but, more importantly, requires only the object's projection images for training rather than its real 3D images, which undoubtedly holds significant application value for the SVCT inverse problem.

Despite its advantages, the reconstruction quality and efficiency of NeRF-based methods remain suboptimal under sparse-view conditions. (1) While recent approaches improve SVCT reconstruction by pretraining implicit neural representation (INR) networks with approximate priors, which are typically derived from similar anatomical regions of different individuals or time points, their practical application in engineering settings is limited. To address this challenge, we introduce the term 'target prior'—priors estimated directly from the object's projection data—which are more accessible and relevant, providing object-specific information that enhances sparse-view reconstruction. (2)

Current methods often utilize positional encoding to implicitly learn voxel-wise intensity distributions, which can result in insufficient resolution and severe artifacts due to inadequate supervision. To address these issues, We enhance implicit feature representations by incorporating structural encoding from target priors for each voxel. This dual encoding strategy enhances discriminative representation and improves reconstruction accuracy, particularly in sparse-view scenarios. (3) Most implicit CT reconstruction methods use uniform voxel sampling for rendering, potentially leading to insufficient sampling of challenging regions. We optimize the sampling strategy with structural guidance from target priors, adaptively focusing on the most critical and challenging regions. This targeted sampling improves voxel efficiency for loss calculation, thereby enhancing overall learning outcomes.

With these solutions, we propose TPG-INR, a novel implicit CT reconstruction framework designed to enhance current sparse-view imaging techniques and address the identified research challenges mentioned above. Fig. 1 presents a qualitative and quantitative comparison of our method against the state-of-the-art models: NeRP, NAF, and SAX-NeRF, focusing on implicit 3D SVCT chest reconstruction over different durations. The main contributions of our work can be summarized as follows:

- We developed a CUDA-based Target Prior Estimator (TPE) that quickly generates high-quality target priors from an object's projection data. This advancement enhances its practical utility and delivers object-specific relevant priors for INR learning in CT reconstruction.
- We propose a Target Prior-guided Voxel Sampling (TPVS) strategy that utilizes object-specific priors for adaptive sampling. This approach ensures thorough sampling of challenging regions while minimizing the sampling of non-informative areas, enhancing learning efficiency by concentrating resources where they are most needed.
- We enrich the voxel-wise feature representation by integrating structural encoding, which boosts implicit learning capabilities under sparse-view conditions. The structural encoding is derived from the estimated target priors using a Target Prior Structural Encoder (TPSE) module.

2. Related Works

2.1. Implicit 3D Reconstruction

NeRF [21] learns volumetric density and color at different spatial locations through implicit functions, achieving notable success in 3D reconstruction tasks. Following NeRF, several studies have applied it to medical imaging. Zha et al.'s NAF [38] and Cai et al.'s SAX-NeRF [5] retain the raybased training strategy from NeRF, using multi-scale hash encoding for positional representation to accelerate convergence. However, their reconstructed results capture lim-

ited intricate medical details under ultra-sparse view projection. Additionally, Shen et al.'s NeRP [27], Zang et al.'s IntraTomo [37], and M. Tancik et al.'s GRFF [34] have each developed unique medical imaging reconstruction models inspired by NeRF principles. They employ Gaussian Fourier encoding and treat the entire object as the training unit. While these approaches have demonstrated commendable results with sparse-view projections, they sacrifice time efficiency in the process.

2.2. Strategy of Ray Sampling

To enhance the training and rendering efficiency of NeRF, many sampling optimization methods focus on minimizing the number of sampling points along the rendering rays. Techniques such as TermiNeRF [25], NeuSample [7], and DONeRF [22] utilize a joint training approach, where a sampling neural network is trained alongside the main model. This allows for a single network inference per ray during rendering to determine all necessary sampling positions. EfficientNeRF [13] employs a coarse-to-fine sampling strategy akin to NeRF, but it only computes valid samples with a density greater than zero during the coarse sampling phase. While these methods prioritize rendering speed by reducing the number of samples, they often compromise reconstruction quality.

2.3. Prior-based Implicit Reconstruction

To enhance reconstruction quality under sparse-view projections, Shen et al. introduced NeRP [27], which leverages prior CT images from previous scans of the same patient for network pre-training. This approach requires only a few projections during sparse-view conditions, allowing for high-quality reconstructions through self-supervised training. Du et al. introduced DPER [6], which uses a large amount of approximate prior data to train a diffusion model. The noisy intermediate results from the diffusion model serve as pre-trained prior information, guiding the network training and producing reasonably good results. However, the prior data required by these methods is not always easily accessible, which limits their practical applicability.

3. Methodology

3.1. Overall Framework

As shown in Fig. 2 (a), our implicit CT reconstruction model takes projection data (I_{gt}) as input. It first uses the TPE algorithm to quickly generate the target prior (\hat{T}) . This prior guides the Target Prior-guided Voxel Sampling (TPVS) module, which efficiently samples voxels along rays for implicit representation learning, as detailed in Fig. 2 (b) and Sec. 3.3. Each sampled voxel is defined as p = (x, y, z), with (x, y, z) representing its 3D coordinates along ray r. To prevent local optima, rays R_s are randomly selected from the

cone-beam imaging system for voxel sampling. The sampled voxels (p) from all selected rays (R_S) are then encoded by the positional encoder E_P and the structural encoder E_S for voxel-wise implicit representation and reconstruction.

The Positional Encoder (E_P) transforms voxel coordinates (x, y, z) using a Gaussian Fourier encoder γ , which effectively captures complex medical details [34] and is defined as:

$$\gamma(p) = [\sin(2\pi Bp), \cos(2\pi Bp)] \tag{1}$$

Here, $B \sim N(a, c^2)$ acts as a scaling factor for the positional encoding. The encoded coordinates $\gamma(p)$ are further optimized through a two-layer multi-layer perceptron (MLP) network (f_p) , yielding the positional encoding F_p :

$$F_p = E_P(x, y, z) = f_p(\gamma(p); \phi_1)$$
 (2)

The Structural Encoder E_S is implemented using our Target Prior Structural Encoder (TPSE) module, as shown in Fig. 2 (c). It queries the intensity value from the target prior \hat{T} at position p=(x,y,z) to obtain the voxel-specific prior intensity \hat{t}_p and its neighboring structure $Q_{n\times n\times n}(\hat{t}_p)$. A two-layer MLP then encodes the structure, obtaining the structural encoding F_S as follows:

$$F_S = E_S(\hat{T}, p) = f_S(Q_{n \times n \times n}(\hat{t}_p); \phi_2) \tag{3}$$

Here, f_s denotes the two-layer MLP network, while ϕ_2 represents its learnable parameters.

The positional and structural encodings (F_p and F_s) are concatenated and input into a MLP network, denoted as f_{INR} with parameters ϕ_3 , for implicit learning. This network predicts the radiance density σ for each voxel sampled along the randomly selected rays (R_s):

$$\sigma = f_{INR}(\text{Concat}(F_p, F_s); \phi_3) \tag{4}$$

The INR reconstruction network utilizes periodic activation functions after each fully connected layer to capture high-frequency signal details [31]. To ensure non-negative predictions consistent with the absorption properties of X-rays, a Sigmoid function is applied in the final layer.

By leveraging the Beer-Lambert law [33] for penetrated CT imaging and rendering, we can express the multi-view projection along a ray r as follows:

$$I_{\text{pred}}(r) = \mathcal{M}_{\theta}(\sigma, r) = I_0 \cdot \left(1 - e^{-\sum_{p=1}^{N} \sigma_p t_p}\right)$$
 (5)

In this equation, σ_p represents the predicted radiance density at voxel coordinate p, while t_p indicates the distance between two adjacent voxels. Here, N is the total number of voxels along the ray path r. We define $\mathcal{M}_{\theta}(\sigma, r)$ as the projection function of the ray r in the θ direction, which

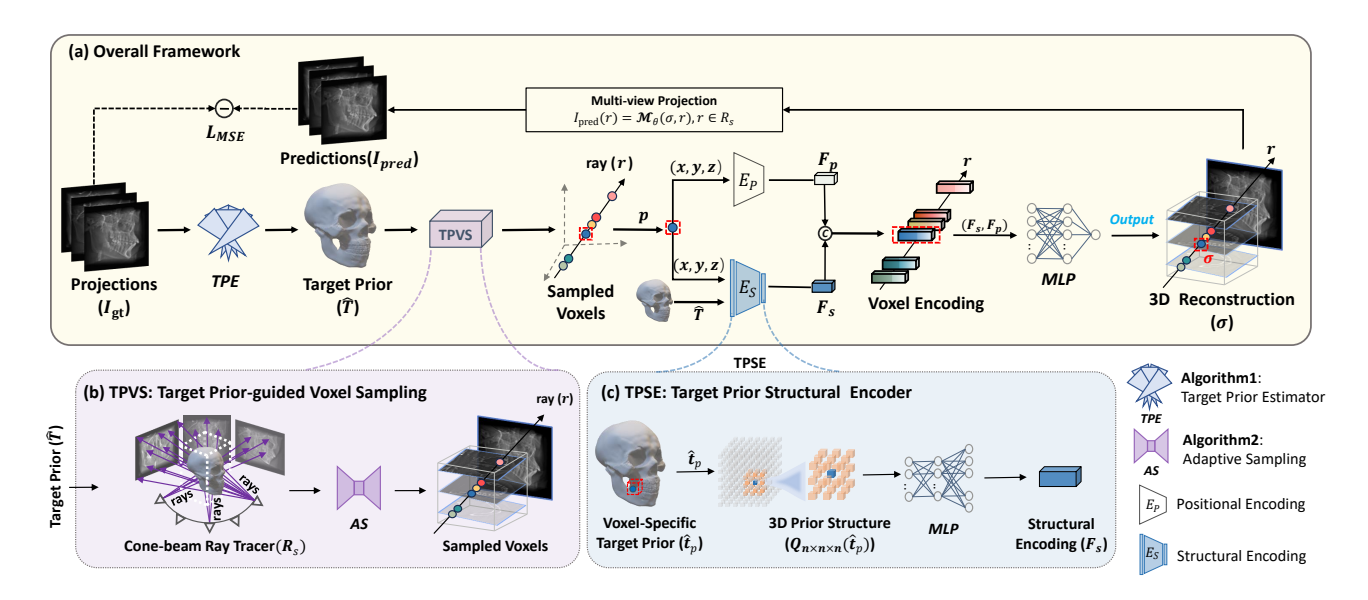


Figure 2. Overview of the TPG-INR 3D CT Reconstruction Network. (a) The model takes sparse-view projections as input and outputs a reconstructed 3D volume. It begins by employing the TPE algorithm (see Alg. 1) to estimate a target prior from the input projections. This prior serves as a guiding framework for the TPVS module, which samples voxels along rays to facilitate implicit representation learning. Each sampled voxel is encoded with both positional information and prior-based structural details, denoted as E_p and E_s , respectively. These encoded features are then integrated to form a voxel-wise implicit neural representation, enabling the reconstruction of the CT image volume. The reconstructed volume is subsequently utilized for loss calculation through multi-view projection. (b) Illustration of the TPVS module, which leverages the target prior to guide voxel sampling along rays. (c) Detailed view of the TPSE module, which utilizes the target prior for voxel-wise structural encoding.

intersects an object with radiance densities of σ . The corresponding values in the prediction domain are denoted as $I_{\text{pred}}(r)$.

To facilitate self-supervision during model training, we compute the L2 loss between the predicted projections of all selected rays and the corresponding ground truth at the pixel level as cost function, expressed by:

$$L_{\text{MSE}} = \frac{1}{|R_s|} \sum_{r \in R_-} ||I_{\text{pred}}(r) - I_{\text{gt}}(r)||_2^2$$
 (6)

3.2. Target Prior Estimator

The TPE algorithm (see Alg. 1) enables rapid and high-quality target prior estimation, leveraging iterative reconstruction on CUDA. It initializes the target prior \hat{T} to zero. In each iteration, random rays are selected from the cone-beam imaging system using the operation Random(), forming a ray subset R_s for the current estimation. The voxel-wise update for \hat{T} along these rays is defined as:

$$\mu = \nabla f \cdot \operatorname{step}_p + \lambda_1 \cdot LV(\hat{t}_p), p \in R_s^j. \tag{7}$$

Here, ∇f is the difference between the estimated projection and the ground truth along the selected rays, serving as the gradient for updating \hat{T} . To address uneven voxel sampling

Algorithm 1 TPE: Target Prior Estimator

```
Input: I_{gt}, K, \lambda_1; \mathcal{M}_{\theta}()
  1: Initialize \hat{t} = \text{Count} = T \in \mathbb{R}^3, \nabla f = T \in \mathbb{R}
  2: for j = 1, ..., K do
               Use Random to select rays:
  3:
               R_s^j = Random(I_{gt})
  4:
               I_{\text{pred}}(R_s^j) = \mathcal{M}_{\theta}(\hat{t}^j, R_s^j)
  5:
               Calculate the selected rays' projection losses:
  6:
               \nabla f = I_{\text{pred}}(R_s^j) - I_{\text{gt}}(R_s^j)
  7:
               Determine voxels' update rate along selected rays:
               step<sub>p</sub> = \frac{\max(\operatorname{Count}^j)}{\operatorname{Count}^j_p}, p = (x, y, z) \in R^j_s
Compute the update gradient for voxels:
  9:
10:
               \mu = \nabla f \cdot \text{step}_p + \lambda_1 \cdot LV(\hat{t}_p^j), p \in R_s^j
11:
               Update the target prior for the voxels: \hat{\mathbf{t}}_p^{j+1} = \hat{\mathbf{t}}_p^j + \mu, p \in R_s^j
12:
13:
               Update the sampling count for the voxels:

\operatorname{Count}_{p}^{j+1} = \operatorname{Count}_{p}^{j} + 1, p \in R_{s}^{j}
14:
15:
Output: \hat{\mathbf{T}} = \hat{\mathbf{t}}^K
```

that may lead to varying convergence rates and local optima, we introduce an adaptive update rate, step_p , defined as: $\text{step}_p = max(\text{Count}^j)/\text{Count}_p^j$. This ratio adjusts the update rate for each voxel p based on its sampling count relative to the maximum across all voxels, ensuring a more

balanced convergence across the dataset.

Inspired by Total Variation (TV) regularization in SART-TV [36], we note that most regions in medical imaging (excluding boundaries) exhibit low Local Variation (LV). To improve prior estimation, we integrate LV into the update process. The local variation at voxel coordinates *p* is defined as:

$$LV(\hat{t}_p) = \operatorname{aver}(Q_{m \times m \times m}(\hat{t}_p)) - \hat{t}_p \tag{8}$$

where \hat{t}_p is the estimated target prior of p, and $(Q_{m \times m \times m}(\hat{t}_p))$ represents its m-sized neighboring priors. The 'aver' function computes the average of these neighbors. By incorporating LV as a regularization term, the iteration process smooths the final result by reducing high-frequency noise while preserving structural information. Our TPE algorithm aims to provide high-quality structural priors, while precise high-frequency details are captured by the overall INR network. Filtering high-frequency noise using the LV component enhances network training by minimizing potential disruptions.

The proposed TPE algorithm provides high-quality target prior estimation in a short timeframe, typically within tens of seconds. This temporal efficiency is achieved through its CUDA-based parallelized implementation. The algorithm's quality advantage is attributed to two main factors: first, an adaptive gradient update applied to ∇f , which ensures stable convergence; and second, the integration of local variation (LV), which suppresses noise and guarantees a high-fidelity estimation.

3.3. Target Prior-guided Voxel Sampling

The INR learning strategy based on ray tracing treats each voxel as an independent learning unit, enabling improved training efficiency through an optimized sampling strategy. Fig. 3 illustrates three voxel sampling strategies using the brain as an example. The Uniform Sampling strategy, shown in Fig. 3(a), provides broad coverage across the entire space; however, it may lead to ineffective sampling in both background and non-informative foreground regions, often neglecting the most challenging areas crucial for efficient learning. This method is commonly used in current NeRF-based CT reconstruction models. The Boundary-Constrained Uniform Sampling strategy, depicted in Fig. 3(b), samples voxels evenly within the cubic boundary but still falls short in prioritizing on informative regions. In contrast, the Structural-Guided Sampling, illustrated in Fig. 3(c), represents a more targeted approach. This strategy ensures concentrated sampling of challenging regions while minimizing the sampling of non-informative areas. This strategy enhances the loss gradient for model training, making it more effective for efficient learning.

We propose the Target Prior-guide Voxel Sampling (TPVS) module to enhance learning efficiency through the

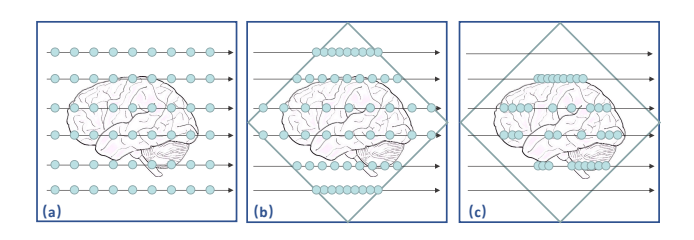


Figure 3. Comparison of three different sampling strategies. (a) Uniform Sampling: even voxel selection across space; (b) Boundary-Constrained Uniform Sampling: even selection restricted to defined boundaries; (c) Structural-Guided Sampling: optimized voxel distribution based on structural information.

Algorithm 2 AS: Adaptive Sampling

```
Input: P, D, f(x, y, z); N_{dropout}
      1: Sequentially remove unnecessary N_{\text{dropout}} points:
      2: Initialize P = \overline{P}, D = \overline{D}
      3: for \ell = 1, \ldots, N_{\text{dropout}} do
                                     Find voxel in P that has the minimum field value:
      4:
                                      P_i = \text{FindMin}(P, f(x, y, z))
       5:
                                      Determine whether it is a background area:
      6:
      7:
                                      if f(P_i) = 0 then
      8:
                                                         Remove the sampled voxel:
                                                        P_i = False, D_i = False
      9:
  10:
                                      else
                                                      Adaptively allocate intervals to its neighbors: D_{i+1} = \left(1 - \frac{|f(P_i) - f(P_{i+1})|}{|f(P_i) - f(P_{i+1})| + |f(P_i) - f(P_{i-1})|}\right) \cdot D_i
D_{i-1} = \left(1 - \frac{|f(P_i) - f(P_{i-1})|}{|f(P_i) - f(P_{i-1})| + |f(P_i) - f(P_{i-1})|}\right) \cdot D_i
Demons the semi-less state of 
  11:
  12:
  13:
                                                        Remove the sampled voxel:
  14:
  15:
                                                         P_i = False, D_i = False
                                                         Update the sampling field:
  16:
 17:
                                                         f(P_i) += \lambda_2 \cdot f(P_i)
  18:
                                     end if
  19: end for
```

20: ℓ denotes the iteration; i is the index of sampled points in P.

Output: return P, D

Structural-Guided Sampling strategy. As shown in Fig. 2(b), TPVS employs the target prior (\hat{T}) to guide the sampling process, thereby providing structural information. It treats adaptive voxel sampling as a dynamic optimization problem involving voxel positions (P) and their distance intervals (D) along selected rays (R_s) , formulated as:

$$P, D = AS(\overline{P}, \overline{D}, f(x, y, z))$$
(9)

Here, \overline{P} and \overline{D} denote initial voxel positions and intervals based on a dense uniform distribution along each ray. The sampling field f(x, y, z) is derived from our target priors (\hat{T}) using:

$$f(x, y, z) = \beta \cdot grad(\hat{T}) + (1 - \beta) \cdot \hat{T}$$
 (10)

In this equation, $grad(\hat{T})$ represents the gradient magnitude of the priors, and β balances the contributions of the prior

and its gradient. This sampling field f(x, y, z) distinguishes the challenging regions from the non-informative ones by combining both target priors and their derivatives, providing comprehensive evidence for the identification of complex structures.

With initial voxel positions $(\overline{P} = \{p_1, p_2, ..., p_n\})$, distance intervals $(\overline{D} = \{d_1, d_2, ..., d_n\})$, and the sampling field f(x, y, z), our TPVS strategy implements the position optimization process through the Adaptive Sampling (AS()) in Eq. 9) algorithm, as detailed in Alg. 2. The algorithm executes N_{dropout} iterations, removing one sampled point from P per iteration. In each iteration, it assesses the structural complexity of the sampled point using the sampling field f(x, y, z) and adaptively assigns distance intervals to its neighbors along a ray. This approach prioritizes the removal of non-informative points, resulting in a concentrated voxel sampling distribution in challenging regions for implicit learning.

4. Experiment

4.1. Experimental Settings

Dataset: Experiments were conducted using the datasets that include jaw, chest, abdominal, and foot regions. The chest dataset is sourced from the LIDC-IDRI dataset [1], while the remaining datasets come from Open Scientific Visualization Datasets [18]. To explore the model's robustness across different data distributions, all datasets were rescaled to dimensions of $128 \times 128 \times 40$. The ground-truth projections were generated by our CUDA implementation of projector \mathcal{M}_{θ} with imaging parameters referring to TIGRE [3].

Implementation Details: Our model is implemented using PyTorch [24], with CUDA version 10.1 [23]. We use the Adam optimizer with a fixed learning rate of 0.00001. In the TPE algorithm, $\lambda_1 = 0.001$, m = 3 for the LV calculation, and each ray is sampled by P = 192 voxels, as determined by our experimental study. To extract target priors, the neighboring size n = 5. The iteration number for fast prior estimation is set as K = 50. In the TPVS module, the initial sampling size P is set to 216, requiring the AS algorithm to discard $N_{\text{dropout}} = 24$ samples per ray. The contribution coefficient of the target prior and its derivatives is set to $\beta = 0.2$, while the algorithm parameter λ_2 is set to 0.5. All experiments are conducted on an RTX 3090 GPU. Ultrasparse view projection is implemented using 10, 20, and 30 views, with 100 iterations, where each iteration samples all rays once. The quality of reconstruction is evaluated using Peak Signal-to-Noise Ratio (PSNR) [12] and Structural Similarity Index Measurement (SSIM) [14].

4.2. Comparison Results

Quantitative Results on Quality: As illustrated in Tab. 1, we provide a quantitative comparison of various reconstruc-

tion methods applied to different body regions under several sparse-view scenarios. The methods evaluated include traditional analytical reconstruction techniques, such as FBP [16] and FDK [8], iterative methods like SART-TV [36], and implicit learning-based methods, namely NeRP[27], NAF[38], and SAX-NeRF[5]. For the NeRP method, we adopt the non-prior version, tailored to practical reconstruction scenarios where only the projection data of the object itself is available. The experimental results presented in the table indicate that our method achieve notably higher reconstruction quality in both 2D parallel-beam and 3D cone-beam configurations, with a particularly significant advantage in the 3D cone-beam setup. For instance, in the case of the chest and abdomen datasets using a 20-angle cone-beam configuration, our method surpasses the current state-ofthe-art NeRP, achieving improvements in PSNR of 4.89 dB and 5.42 dB, respectively.

Visual Results on Quality: In Fig. 4, we present the visual comparisons of different methods for 3D cone-beam reconstruction. It is evident that our method achieves the best visual performance across all datasets and significantly outperforms other approaches. Specifically, FDK reconstruction exhibits low image quality with severe artifacts, as analytical methods require dense angular sampling of projection data. The iterative method SART-TV suppresses noise but sacrifices fine details and performs poorly under sparse projection conditions. NeRP, when deprived of its approximate prior, suffers from artifacts and blurring when reconstructing from sparse-view projections. Although NAF and SAX-NeRF mitigate some artifacts present in NeRP, the overall image quality remains suboptimal, with persistent noise and missing structural details. In contrast, by incorporating the TPVS and TPSE modules, the proposed method preserves finer details and effectively suppresses artifacts, thereby achieving superior reconstruction fidelity.

Comparisons on Time Efficiency: In practical CT imaging systems, reconstruction time is a critical performance metric. Fig. 5 presents comparisons of Time-PSNR for NeRP, NAF, SAX-NeRF, and our method, all reconstructed using 20 projections across four 3D anatomical regions. Our method demonstrates the shortest reconstruction time while achieving a higher PSNR value. This efficiency can be attributed to two key factors. First, we employ a tailored framework that integrates a ray-based training strategy with a larger network architecture, which enhances both learning efficiency and reconstruction accuracy. Second, our voxel sampling strategy, implemented through the TPVS module, significantly improves the time efficiency of the reconstruction process.

4.3. Ablation Study

Incremental Study: To evaluate our model's effectiveness in enhancing reconstruction performance, we conducted ab-

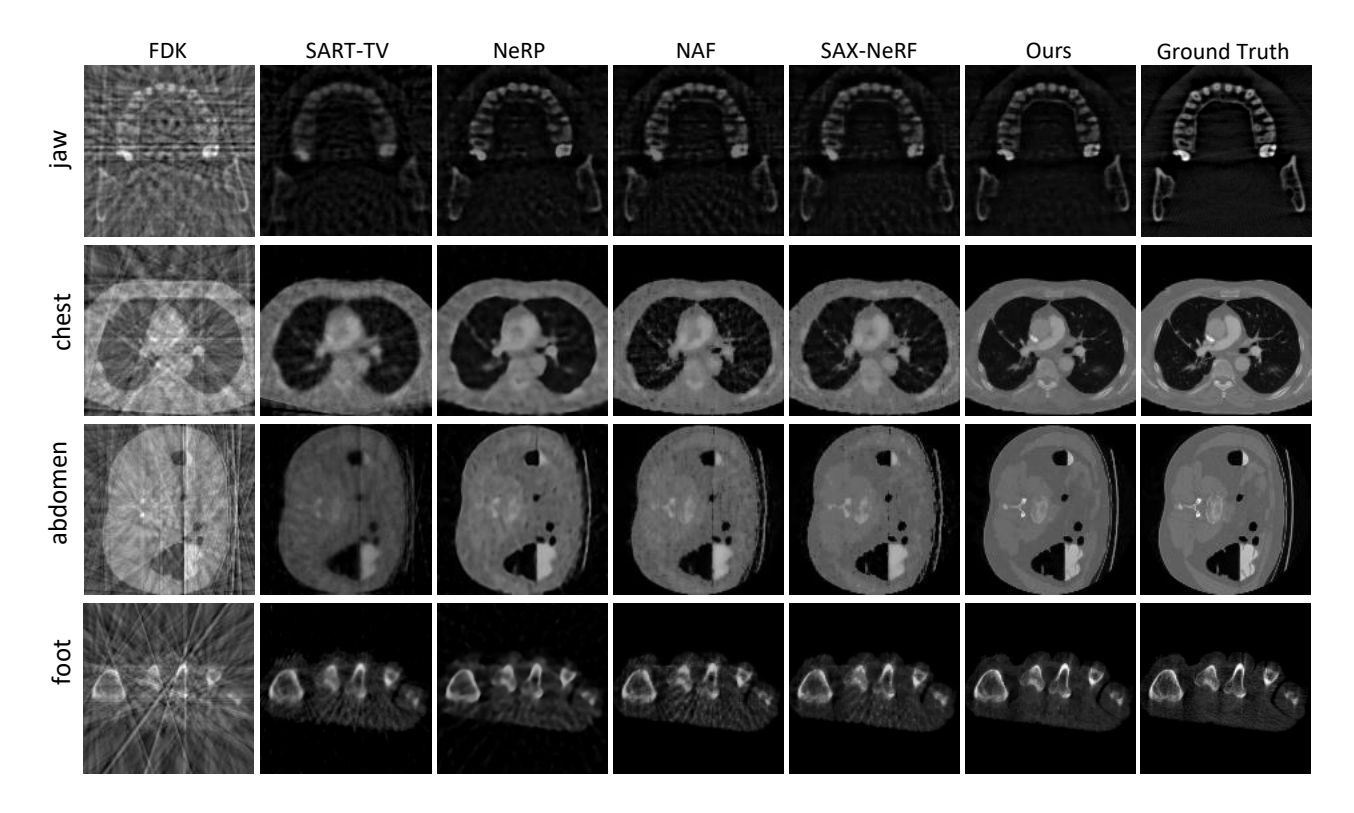


Figure 4. Visual comparison of reconstructed images generated from various 3D CT reconstruction methods, applied to datasets from the jaw, chest, abdomen, and foot. Each reconstruction was based on 20 projection images, highlighting the differences in quality and detail across the different anatomical regions and methods used.

Table 1. Quantitative comparison of reconstructed results from various methods applied to jaw, chest, abdomen, and foot datasets. The experiments were conducted using both parallel 2D and cone-beam 3D imaging techniques under different sparse-view projections.

Data	Views	PSNR/SSIM									
		2D Parallel-beam Reconstruction				3D Cone-beam Reconstruction					
		FBP	SART-TV	NeRP	TPG-INR	FDK	SART-TV	NeRP	NAF	SAX-NeRF	TPG-INR
Jaw	10	19.61/.341	25.64/.710	22.18/.415	25.73/.776	20.40/.440	25.90/.725	28.17/.821	26.04/.750	26.59/.775	29.81/.873
	20	24.06/.594	28.26/.799	23.92/.506	30.19/.877	24.15/.616	28.61/.834	31.85/.912	29.59/.879	29.93/.888	33.90/.945
	30	27.49/.756	30.86/.874	27.69/.723	32.73/.926	26.75/.726	30.94/.895	34.48/.951	31.38/.920	32.42/.934	37.39/.974
Chest	10	17.36/.383	22.22/.727	23.86/.584	26.77/.859	15.56/.360	22.48/.727	26.83/.824	24.50/.787	24.44/.784	28.74/.899
	20	22.41/.602	25.60/.822	27.29/.724	31.82/.936	20.99/.550	25.56/.836	30.66/.913	27.93/.882	27.32/.873	35.55/.974
	30	25.58/.742	27.59/.870	28.37/.791	34.44/.960	24.24/.663	27.59/.889	31.75/.935	30.01/.925	29.80/.919	38.50/.986
Abdomen	10	17.48/.375	22.55/.798	21.11/.489	26.05/.855	16.72/.393	22.83/.794	25.20/.791	24.98/.803	24.80/.826	28.77/.901
	20	21.91/.574	26.17/.833	23.25/.567	29.86/.920	21.06/.535	25.09/.786	30.74/.918	28.20/.882	28.40/.899	36.16/.972
	30	24.58/.708	28.36/.876	24.55/.674	34.24/.955	23.92/.636	28.47/.884	32.95/.947	29.81/.911	30.01/.921	38.65/.981
Foot	10	17.35/.233	25.45/.833	21.91/.404	28.51/.887	17.92/.358	26.20/.854	26.97/.778	25.37/.856	27.20/.890	30.87/.934
	20	22.14/.450	28.57/.884	25.27/.494	32.30/.936	22.04/.439	29.31/.911	30.90/.889	29.15/.920	30.06/.932	35.12/.970
	30	25.43/.640	31.19/.927	28.35/.733	34.51/.955	24.92/.527	31.89/.946	33.03/.936	32.88/.957	32.62/.958	37.27/.981

lation experiments using chest CT data. We separately assessed the TPSE and TPVS modules to determine their contributions to reconstruction quality in 3D cone-beam imaging. Results in Tab. 2 demonstrate that our baseline model achieves reasonable performs across various ultrasparse view projections, thanks to a specialized network designed for efficient medical imaging. The baseline employed a uniform sampling scheme (see Fig. 3(a)) and utilized only positional encoding F_p for implicit learning. For

module evaluation, using 20 views, the TPSE module improved PSNR by 0.65 dB, while the TPVS module enhanced it by 4.76 dB. When both modules were integrated into the baseline, we observed an overall PSNR improvement of 7.55 dB in the 20-view 3D cone-beam reconstruction task. These findings consistently highlight the effectiveness of our network design and the target prior-guided modules in enhancing reconstruction performance.

TPSE module and TPE Algorithm: Tab. 3 shows that

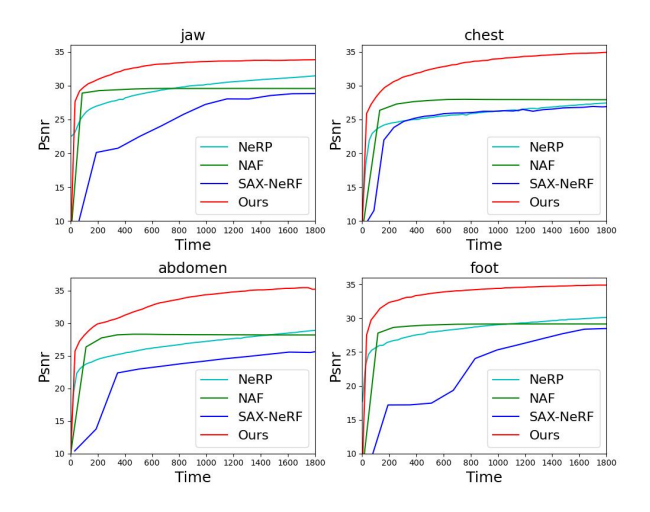


Figure 5. Comparative analysis of learning efficiency by PSNR-Time (s) across various methods and anatomical structures.

Table 2. Incremental Ablation: Evaluating the effectiveness of TPG-INR and its components - the TPSE and TPVS modules.

baseline	TPSE	TPVS	10	20	30
$\overline{}$				28.00/0.911	
\checkmark	\checkmark		25.58/0.826	28.65/0.912	29.46/0.938
\checkmark		\checkmark		32.76/0.954	
	$\sqrt{}$	$\sqrt{}$	28.74/0.899	35.55/0.974	38.50/0.986

incorporating the TPSE module for structural encoding enhances reconstruction accuracy. In this section, we evaluate the generalization performance of structural encoding by replacing the TPE algorithm with traditional methods like FDK and SART-TV, which also derive priors from projections. The reconstruction results σ presented in Tab. 3 indicate that incorporating structural encoding with various prior estimation algorithms improves accuracy compared to the results without the TPSE module, confirming the generalization capability of structural encoding. Notably, our TPE algorithm consistently surpasses the other methods in both prior estimation and image reconstruction, as evidenced by the metrics \hat{t} and σ . This success is attributed to TPE's adaptive gradient updating strategy for efficient learning and the incorporation of LV to suppress noise.

Table 3. Ablation Study: Evaluating the reconstruction accuracy of target prior generated by our TPE algorithm in comparison to the priors produced by traditional reconstruction methods.

Views	Prior/Pred	w/o TPSE	FDK	SART-TV	TPE
10	Î	-	15.56/0.360	22.48/0.727	25.05/0.804
	σ	28.11/0.883	28.31/0.886	28.43/0.889	28.74/0.899
20	Î	-	20.99/0.550	25.56/0.836	28.88/0.903
	σ	32.76/0.954	33.45/0.962	34.48/0.968	35.55/0.974
30	Î	-	24.24/0.663	27.59/0.889	31.69/0.946
	σ	34.91/0.971	35.79/0.978	37.12/0.981	38.50/0.986

TPVS module: In this section, we evaluate the effectiveness of TPVS by comparing its reconstruction efficiency against uniform sampling, which is commonly used in existing models such as NAF and SAX-NeRF. Our comparison involves varying the number of sampled voxels per ray, using chest imaging data with 10, 20, and 30 projection views. As illustrated in Fig. 6, the experiments show that TPVS significantly outperforms uniform sampling across all sampling points and sparse-view scenarios. Additionally, while increasing the number of sampling points improves reconstruction accuracy, it also extends convergence time. To achieve an optimal balance between time efficiency and accuracy, we selected 192 sampled voxels per ray for priorguided sampling and voxel encoding in our reconstruction model.

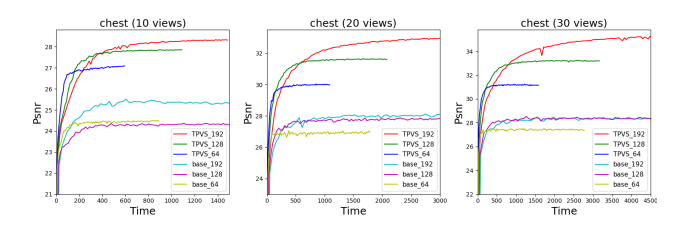


Figure 6. Ablation Study: Evaluating the learning efficiency of our TPVS strategy versus uniform sampling, using varying numbers of sampling voxels per ray over 100 iterations.

5. Conclusions

In this paper, we present TPG-INR, an innovative implicit neural representation model designed for sparse-view CT reconstruction. By utilizing a target prior estimator, our method enables rapid generation of priors from projection data, enhancing voxel-wise feature encoding and voxel sampling for implicit learning. This integrated approach significantly improves reconstruction accuracy and learning efficiency, distinguishing TPG-INR from existing models. Empirical evaluations show that TPG-INR consistently outperforms current methods both quantitatively and qualitatively. Thus, TPG-INR emerges as a leading solution for reconstruction accuracy and efficiency across diverse datasets, advancing CT reconstruction techniques and paving the way for further research in implicit neural representations.

Acknowledgements

This work is supported by the National Natural Science Foundation of China Youth Found under Grant 62202391.

References

- [1] Samuel G Armato III, Geoffrey McLennan, Luc Bidaut, Michael F McNitt-Gray, Charles R Meyer, Anthony P Reeves, Binsheng Zhao, Denise R Aberle, Claudia I Henschke, Eric A Hoffman, et al. The lung image database consortium (lidc) and image database resource initiative (idri): a completed reference database of lung nodules on ct scans. *Medical physics*, 38(2):915–931, 2011. 6
- [2] Ishak Ayad, Nicolas Larue, and Maï K. Nguyen. Qn-mixer: A quasi-newton mlp-mixer model for sparse-view ct reconstruction, 2024.
- [3] Ander Biguri, Manjit Dosanjh, Steven Hancock, and Manuchehr Soleimani. Tigre: a matlab-gpu toolbox for cbct image reconstruction. *Biomedical Physics & Engineering Express*, 2(5):055010, 2016. 6
- [4] David J Brenner and Eric J Hall. Computed tomography—an increasing source of radiation exposure. *New England journal of medicine*, 357(22):2277–2284, 2007. 2
- [5] Yuanhao Cai, Jiahao Wang, Alan Yuille, Zongwei Zhou, and Angtian Wang. Structure-aware sparse-view x-ray 3d reconstruction. In *Proceedings of the IEEE/CVF Conference* on Computer Vision and Pattern Recognition, pages 11174– 11183, 2024. 1, 2, 6
- [6] Chenhe Du, Xiyue Lin, Qing Wu, Xuanyu Tian, Ying Su, Zhe Luo, Rui Zheng, Yang Chen, Hongjiang Wei, S. Kevin Zhou, Jingyi Yu, and Yuyao Zhang. Dper: Diffusion prior driven neural representation for limited angle and sparse view ct reconstruction, 2024. 3
- [7] Jiemin Fang, Lingxi Xie, Xinggang Wang, Xiaopeng Zhang, Wenyu Liu, and Qi Tian. Neusample: Neural sample field for efficient view synthesis, 2021. 3
- [8] Lee A Feldkamp, Lloyd C Davis, and James W Kress. Practical cone-beam algorithm. *Josa a*, 1(6):612–619, 1984. 6
- [9] Jürgen Frikel and Eric Todd Quinto. Characterization and reduction of artifacts in limited angle tomography. *Inverse Problems*, 29(12):125007, 2013.
- [10] EJ Hall and DJ Brenner. Cancer risks from diagnostic radiology. *The British journal of radiology*, 81(965):362–378, 2008.
- [11] Yoseob Han and Jong Chul Ye. Framing u-net via deep convolutional framelets: Application to sparse-view ct. *IEEE transactions on medical imaging*, 37(6):1418–1429, 2018. 2
- [12] Alain Hore and Djemel Ziou. Image quality metrics: Psnr vs. ssim. In 2010 20th international conference on pattern recognition, pages 2366–2369. IEEE, 2010. 6
- [13] Tao Hu, Shu Liu, Yilun Chen, Tiancheng Shen, and Jiaya Jia. Efficientnerf: Efficient neural radiance fields, 2022. 3
- [14] Sung-Wook Hwang and Junji Sugiyama. Computer vision-based wood identification and its expansion and contribution potentials in wood science: A review. *Plant Methods*, 17(1): 47, 2021. 2, 6
- [15] Kyong Hwan Jin, Michael T McCann, Emmanuel Froustey, and Michael Unser. Deep convolutional neural network for inverse problems in imaging. *IEEE transactions on image* processing, 26(9):4509–4522, 2017. 2
- [16] Avinash C Kak and Malcolm Slaney. Principles of computerized tomographic imaging. SIAM, 2001. 2, 6

- [17] Kyungsang Kim, Jong Chul Ye, William Worstell, Jinsong Ouyang, Yothin Rakvongthai, Georges El Fakhri, and Quanzheng Li. Sparse-view spectral ct reconstruction using spectral patch-based low-rank penalty. *IEEE transactions on medical imaging*, 34(3):748–760, 2014.
- [18] P. Klacansky. Open scientific visualization datasets (2022), 2022. 6
- [19] Hoyeon Lee, Jongha Lee, Hyeongseok Kim, Byungchul Cho, and Seungryong Cho. Deep-neural-network-based sinogram synthesis for sparse-view ct image reconstruction. *IEEE Transactions on Radiation and Plasma Medical Sciences*, 3(2):109–119, 2018. 2
- [20] Yinsheng Li, Ke Li, Chengzhu Zhang, Juan Montoya, and Guang-Hong Chen. Learning to reconstruct computed tomography images directly from sinogram data under a variety of data acquisition conditions. *IEEE transactions on medical imaging*, 38(10):2469–2481, 2019. 2
- [21] Ben Mildenhall, Pratul P Srinivasan, Matthew Tancik, Jonathan T Barron, Ravi Ramamoorthi, and Ren Ng. Nerf: Representing scenes as neural radiance fields for view synthesis. *Communications of the ACM*, 65(1):99–106, 2021.
- [22] T. Neff, P. Stadlbauer, M. Parger, A. Kurz, J. H. Mueller, C. R. A. Chaitanya, A. Kaplanyan, and M. Steinberger. Donerf: Towards real-time rendering of compact neural radiance fields using depth oracle networks. *Computer Graphics Fo*rum, 40(4):45–59, 2021. 3
- [23] NVIDIA, P. Vingelmann, and F.H. Fitzek. Cuda, release: 10.2.89, 2020. 6
- [24] A. Paszke and et al. Pytorch: An imperative style, high-performance deep learning library. In Advances in Neural Information Processing Systems, pages 8024–8035. Curran Associates, Inc., 2019. 6
- [25] Martin Piala and Ronald Clark. Terminerf: Ray termination prediction for efficient neural rendering, 2021. 3
- [26] Leonid I Rudin, Stanley Osher, and Emad Fatemi. Nonlinear total variation based noise removal algorithms. *Physica D:* nonlinear phenomena, 60(1-4):259–268, 1992.
- [27] Liyue Shen, John Pauly, and Lei Xing. Nerp: Implicit neural representation learning with prior embedding for sparsely sampled image reconstruction. *IEEE Transactions on Neural Networks and Learning Systems*, 35(1):770–782, 2024. 1, 3,
- [28] Tiancheng Shen, Xia Li, Zhisheng Zhong, Jianlong Wu, and Zhouchen Lin. R² 2 2-net: Recurrent and recursive network for sparse-view ct artifacts removal. In *Medical Image Com*puting and Computer Assisted Intervention—MICCAI 2019: 22nd International Conference, Shenzhen, China, October 13–17, 2019, Proceedings, Part VI 22, pages 319–327. Springer, 2019. 2
- [29] Emil Y Sidky and Xiaochuan Pan. Image reconstruction in circular cone-beam computed tomography by constrained, total-variation minimization. *Physics in Medicine & Biology*, 53(17):4777, 2008. 2
- [30] Emil Y Sidky, Chien-Min Kao, and Xiaochuan Pan. Accurate image reconstruction from few-views and limited-angle data in divergent-beam ct. *Journal of X-ray Science and Technol*ogy, 14(2):119–139, 2006. 2

- [31] Vincent Sitzmann, Julien Martel, Alexander Bergman, David Lindell, and Gordon Wetzstein. Implicit neural representations with periodic activation functions. *Advances in neural information processing systems*, 33:7462–7473, 2020. 3
- [32] Martin Storath, Andreas Weinmann, Jürgen Frikel, and Michael Unser. Joint image reconstruction and segmentation using the potts model. *Inverse Problems*, 31(2):025003, 2015. 2
- [33] Donald F Swinehart. The beer-lambert law. *Journal of chemical education*, 39(7):333, 1962. 3
- [34] Matthew Tancik, Pratul Srinivasan, Ben Mildenhall, Sara Fridovich-Keil, Nithin Raghavan, Utkarsh Singhal, Ravi Ramamoorthi, Jonathan Barron, and Ren Ng. Fourier features let networks learn high frequency functions in low dimensional domains. *Advances in neural information processing systems*, 33:7537–7547, 2020. 3
- [35] Francisca Vasconcelos, Bobby He, Nalini Singh, and Yee Whye Teh. Uncertainr: Uncertainty quantification of end-to-end implicit neural representations for computed tomography, 2023.
- [36] Hengyong Yu and Ge Wang. A soft-threshold filtering approach for reconstruction from a limited number of projections. *Physics in Medicine & Biology*, 55(13):3905, 2010. 2, 5, 6
- [37] Guangming Zang, Ramzi Idoughi, Rui Li, Peter Wonka, and Wolfgang Heidrich. Intratomo: self-supervised learning-based tomography via sinogram synthesis and prediction. In *Proceedings of the IEEE/CVF International Conference on Computer Vision*, pages 1960–1970, 2021. 3
- [38] Ruyi Zha, Yanhao Zhang, and Hongdong Li. Naf: neural attenuation fields for sparse-view cbct reconstruction. In *International Conference on Medical Image Computing and Computer-Assisted Intervention*, pages 442–452. Springer, 2022. 1, 2, 6
- [39] Zhicheng Zhang, Xiaokun Liang, Xu Dong, Yaoqin Xie, and Guohua Cao. A sparse-view ct reconstruction method based on combination of densenet and deconvolution. *IEEE transactions on medical imaging*, 37(6):1407–1417, 2018. 2